8th International Conference on CFD in Oil & Gas, Metallurgical and Process Industries
SINTEF/NTNU, Trondheim NORWAY *CFD11-121*
21-23 June 2011

IN-LINE OIL-WATER SEPARATION IN SWIRLING FLOW

J.J. SLOT[1]*, **L.J.A.M. VAN CAMPEN**[2]†, **H.W.M. HOEIJMAKERS**[1], **R.F. MUDDE**[2]
[1]University of Twente, Faculty of Engineering Technology, Enschede, The Netherlands
[2]Department of Applied Sciences, Delft University of Technology, The Netherlands

* E-mail: j.j.slot@ctw.utwente.nl
† E-mail: l.j.a.m.vancampen@tudelft.nl

ABSTRACT
An in-line oil-water separator has been designed and is investigated for single- and two-phase flow. Numerical single-phase flow results show an annular reversed flow region. This flow pattern agrees qualitatively with results from measurements. In the two-phase flow simulations two different drag laws have been used to model the interaction between the phases. The velocity field of the single- and the two-phase flow is shown to be very similar. However, the oil volume fraction distribution is strongly affected by the choice of the drag law. Furthermore, compared to experimental results for both drag laws the separation efficiency is greatly overestimated.

Keywords: Oil-water separation, CFD, two-fluid model .

NOMENCLATURE

NOMENCLATURE

Greek Symbols

α	Volume fraction, $[-]$
γ	Volume porosity, $[-]$
θ	Azimuthal coordinate, $[rad]$
μ	Dynamic viscosity, $[kg/ms]$
ν	Kinematic viscosity, $[m^2/s]$
ρ	Mass density, $[kg/m^3]$
σ	Viscous stress tensor, $[kg/ms^2]$

Latin Symbols

C_D	Drag coefficient, $[-]$
D	Droplet diameter, $[m]$
g	Gravitational acceleration, $[m/s^2]$
$\mathbf{K}_{loss}$	Inertial loss coefficients, $[kg/m^2s^2]$
M	Interfacial momentum transfer, $[kg/m^2s^2]$
p	Static pressure, $[kg/ms^2]$
r	Radial coordinate, $[m]$
Re_D	Reynold number, $[-]$
S_M	Momentum loss term, $[kg/m^2s^2]$
$\mathbf{U}$	Instantaneous velocity, $[m/s]$
$\mathbf{u}$	Mean velocity, $[m/s]$
$\mathbf{u}'$	Turbulent velocity fluctuations, $[m/s]$
z	Axial coordinate, $[m]$

Sub/superscripts

θ	Azimuthal
b	Bulk
k	Phase k
m	Mixture
o	Oil
w	Water
z	Axial

INTRODUCTION

The oil market faces an ever increasing worldwide demand for oil, while the number of easily accessible oilfields is decreasing. Therefore, new technologies are required for fields with hydrocarbons that are difficult to produce, such as offshore or sub-sea. Furthermore, as an oil field matures, the crude oil is produced with increasing quantities of water. Therefore, the efficient separation of oil from water becomes an increasingly important processing step. This separation of the phases is required in order to reduce the demands on the transport facilities and to facilitate re-injecting the separated water into the reservoir to maintain the well pressure.
Traditionally, separation is mostly achieved in very large vessels using the action of gravity. However, the large weight and space requirements of these vessels lead to high investment costs for the necessary on-site processing facilities. The present research investigates a much smaller and cheaper alternative for the oil-water separation, namely utilizing in-line equipment that uses swirling flow to separate the phases. Moreover, the smaller equipment size leads to a reduced hydrocarbon inventory. This in turn leads to reduced safety risks. Also, lower costs for maintenance and inspection can be achieved using piping rather than vessels.
Swirling flow has been used successfully for the separation of solids from either gas (Hoekstra, 2000) or liquid (Bradley, 1965). Liquid-liquid separation presents more challenges due to the smaller density difference, high volume fractions of the dispersed phase, poor coalescence and the danger of emulsion formation. Dirkzwager (1996) designed an in-line liquid-liquid separator. Subsequently, single-phase experiments were carried out for this separator. Murphy *et al.* (2007) compared results from these measurements with numerical results from two different commercial CFD packages. It was found that the main features of the flow were qualitatively well represented in the numerical simulations. However, large quantitative differences were observed between the numerical results mutually and between numerical results and experimental data. An oil extraction outlet was added

to the in-line separator by Delfos *et al.* (2004), who further investigated this design numerically.
Much work has been done on single-phase simulations of strongly swirling flow in separators (Ko, 2005; Kharoua *et al.*, 2010). However, the two-phase flow calculations have received less attention. For lower concentrations of the dispersed phase, the behavior of the dispersed phase can be calculated by Lagrangian particle-tracking, see for instance Derken (2003). However, in separators high concentrations of the dispersed phase are often encountered. For these applications, mixture models (Manninen and Taivassalo, 1996) or two-fluid models (Drew, 1983; Prosperetti and Tryggvason, 2007) can be used to predict the flow. Contrary to mixture models, in the two-fluid model for each phase separate continuity and momentum equations are solved. This allows the velocity field of both phases to be different, so that more physics can be incorporated in the simulation. This two-fluid model has more recently been applied to hydrocyclones (Noroozi and Hashemabadi, 2009; Paladino *et al.*, 2007).
The current project aims at the design and investigation, both numerically and experimentally, of an oil-water bulk separator using swirling flow. The intended use is for separation of oil-in-water mixtures with relatively high oil volume fractions. These are mixtures that cannot be considered dilute. For this purpose an in-line separator has been designed and an experimental facility has been built. This paper will discuss the flow patterns observed in the newly designed separator for both single-phase water and two-phase oil-water flows. The single-phase water solution from the computation will be compared to LDA measurements to assess to accuracy of the numerical results. For the two-phase flow two widely used drag law formulations will be used and results will be compared to the experimentally determined separation efficiency.

IN-LINE SWIRL SEPARATOR DESIGN

The present prototype for in-line oil-water separation features a stationary internal swirl element (**ISE**) which is placed within a pipe with a 100 mm internal diameter. This ISE consists of a central body equipped with 9 vanes which are attached to the wall of the pipe and to the surface of the central body, as is shown in figure 1. The incoming flow is accelerated towards the narrow vaned section. The vanes deflect the fluid, generating the swirling flow. The higher axial velocity, and the relatively large radius at which the vanes are placed, both contribute to increases in angular momentum. Downstream of the ISE the strongly swirling flow, with centrifugal forces up to 300 g, will force the lighter oil phase to the center of the pipe where it is collected by a pick-up tube further downstream. Since both water and oil phase flow downstream this is a co-current separator, contrary to the counter-

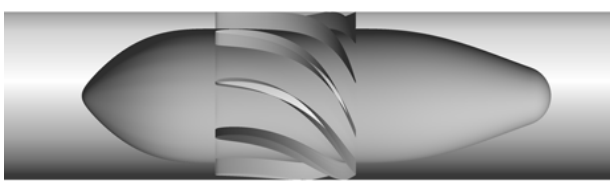

Figure 1: Cut-away of 100 mm diameter pipe showing internal swirl element (ISE). Non-swirling fluid enters from the left.

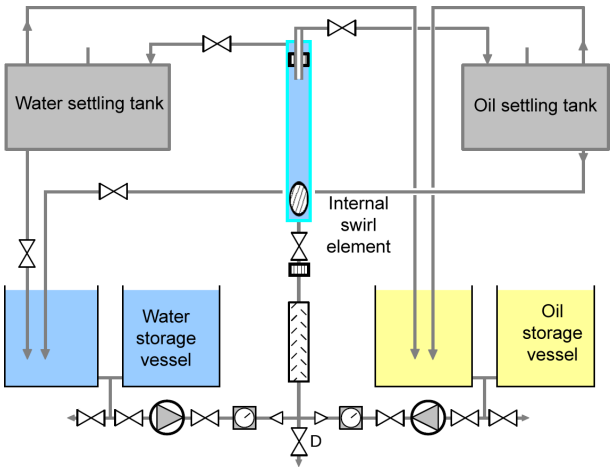

Figure 2: Flow scheme of experimental setup.

current design of Delfos *et al.* (2004). The pick-up tube is placed 1.7 m downstream of the ISE. It is a straight pipe with an outer diameter of 50mm and wall thickness of 1 mm which is concentrically placed within the 100mm diameter pipe.

Experimental setup

At Delft University of Technology an experimental setup of the separator has been built to perform both single and two-phase flow measurements on the separator. The main components can be seen in figure 2. Large storage vessels for water and oil, respectively, feed centrifugal pumps which can produce a mixture of widely varying oil volume fraction. The oil-water mixture passes a static mixer and a flow straightener before it enters the ISE. Downstream of the ISE the stainless steel pick-up tube is placed to collect the bulk of the oil. Subsequently this stream flows into the oil settling tank. In the annular pipe leading to the outlet of the heavier phase, a flow straightener is placed 215 mm downstream of the pick-up tube entrance. This flow straightener eliminates the swirl, which would otherwise lead to air being sucked into the separator from the water settling tank. In the the settling tanks complete separation is achieved and the oil and water flow to their respective storage vessels.
Downstream of the ISE, a Poly Methyl MethAcrylate (PMMA) measurement pipe segment is placed to provide optical access for the Laser Doppler Anemometry (LDA) measurements. The PMMA tube is surrounded by a square box filled with water to reduce refraction of laser light. An Argon laser is used, from which the 488.0 nm beams are used for the axial velocity component and the 514.5 nm beams for the azimuthal velocity component. The burst correlation is conducted in a Dantec F60 BSA signal processor. The average velocity is calculated using a software package developed by Belt (2007), correcting the LDA time-averaged results for white noise, multiple validation and a bias towards high velocities.
The flow through each pump is measured and can be adjusted, additionally a Coriolis flow meter is placed in the pipe leading to the water settling tank. The combination of this data completely determines the flow split and volume fractions of the two outlet flows. Separation efficiencies can be derived from that data.

COMPUTATIONAL FLUID DYNAMICS

The flow field in the new separator design is investigated by solving the Reynolds averaged Navier-Stokes equations for transient incompressible flow.

Single-phase flow

For single-phase flow the governing equations are given by:

$$\nabla.\mathbf{u} = 0 \tag{1}$$

$$\frac{\partial \mathbf{u}}{\partial t} + (\mathbf{u}.\nabla)\mathbf{u} = -\frac{\nabla p}{\rho} + \nu\nabla^2\mathbf{u} + \mathbf{g} - \nabla.\langle \mathbf{u}'\mathbf{u}' \rangle \tag{2}$$

Here ρ is the density, p is the static pressure, $\mathbf{u}$ is the mean velocity and $\mathbf{u}'$ is the turbulent velocity fluctuation. The latter are related to the instantaneous velocity $\mathbf{U}$ as

$$\mathbf{U} = \mathbf{u} + \mathbf{u}' \tag{3}$$

It is assumed that the timescale of the turbulent velocity fluctuation $\mathbf{u}'$ is much smaller than the timescale of the mean velocity $\mathbf{u}$.

The use of eddy-viscosity models to express the Reynolds stresses in term of the mean quantities is not well suited for swirling flow, see Pope (2000). The skewness of the flow violates the eddy-viscosity assumption that the shear stresses and the velocity gradients have the same direction, as pointed out by Kitoh (1991). Various sources of turbulence, i.e. strain rates, are not represented by the eddy viscosity models. Also, the assumption of isotropic turbulence overstates the shear stresses and the radial diffusion of momentum, see Murphy *et al.* (2007).

Therefore a Reynolds stress model (RSM) is used, in which the Reynolds stresses $\langle \mathbf{u}'\mathbf{u}' \rangle$ are provided by transport equations. One of the advantages of the model is that the production terms of the Reynolds stresses can be represented exactly. Therefore, the strain rates associated with streamline curvature and flow skewness, both important in swirling flow, are incorporated in the production of turbulence, see Hanjalic (1999). Moreover, anisotropic behavior of the turbulent flow can be accounted for by the separate transport equations for the Reynolds stresses.

In the present research the SSG Reynolds stress model of Speziale *et al.* (1991) is used. Contrary to other models, this model uses a quadratic pressure-strain relation. This RSM is recommended for swirling flows, e.g. by Cullivan *et al.* (2003) and Chen and Lin (1999). To close the SSG model, a seventh transport equation is included, namely for the dissipation rate.

The Reynolds stress transport equation for an incompressible, isothermal flow is given by

$$\frac{\partial \langle u_i'u_j' \rangle}{\partial t} + \langle u_k \rangle \frac{\partial \langle u_i'u_j' \rangle}{\partial x_k} + \frac{\partial T_{ijk}}{\partial x_k} = P_{ij} + R_{ij} - \varepsilon_{ij} \tag{4}$$

Index notation is used here for convenience. In equation (4) the Reynolds stress flux tensor T_{ijk} is modeled by the gradient-diffusion model of Daly and Harlow (1971):

$$T_{ijk} = \left(\nu\delta_{kl} + C_s \frac{k}{\varepsilon} \langle u_k'u_l' \rangle \right) \frac{\partial \langle u_i'u_j' \rangle}{\partial x_l} \tag{5}$$

The constant C_s = 0.22 and k is the turbulent kinetic energy. P_{ij} is the production tensor which gives the Reynolds stresses generated by the mean flow velocity gradients. It transfers kinetic energy from the mean velocity field to the fluctuation velocity field. The production tensor is given by

$$P_{ij} = -\langle u_i'u_k' \rangle \frac{\partial \langle u_j \rangle}{\partial x_k} - \langle u_j'u_k' \rangle \frac{\partial \langle u_i \rangle}{\partial x_k} \tag{6}$$

The pressure-strain tensor R_{ij} models the redistribution of the energy among the Reynolds stresses and is often split into two contributions; the slow pressure-strain or return-to-isotropy tensor $R_{ij}^{(s)}$ and the rapid pressure-strain tensor $R_{ij}^{(r)}$. In the SSG the $R_{ij}^{(s)}$ tensor is given by

$$R_{ij}^{(s)} = -\varepsilon \left[C_{s1}a_{ij} + C_{s2} \left(a_{ik}a_{kj} - \frac{1}{3}a_{kl}a_{kl}\delta_{ij} \right) \right] \tag{7}$$

Here the constants C_{s1} = 1.7 and C_{s2} = -1.05. The normalized anisotropy tensor a_{ij} is defined as

$$a_{ij} = \frac{\langle u_i'u_j' \rangle}{k} - \frac{2}{3}\delta_{ij} \tag{8}$$

Evidently, $R_{ij}^{(s)}$ is quadratic in the anisotropy tensor. The rapid pressure-strain tensor is given by

$$\begin{aligned} R_{ij}^{(r)} \quad = \quad & -C_{r1}Pa_{ij} + \\ & C_{r2}kS_{ij} - \\ & C_{r3}kS_{ij}\sqrt{a_{kl}a_{kl}} + \\ & C_{r4}k\left(a_{ik}S_{jk} + a_{jk}S_{ik} - 2/3\, a_{kl}S_{kl}\delta_{ij} \right) + \\ & C_{r5}k\left(a_{ik}\Omega_{jk} + a_{jk}\Omega_{ik} \right) \end{aligned} \tag{9}$$

P is the production of turbulent kinetic energy given by

$$P = \langle u_l'u_k' \rangle \frac{\partial \langle u_l \rangle}{\partial x_k} \tag{10}$$

Furthermore, S_{ij} is the mean strain rate tensor, defined by

$$S_{ij} = \frac{1}{2}\left(\frac{\partial \langle u_i \rangle}{\partial x_j} + \frac{\partial \langle u_j \rangle}{\partial x_i} \right) \tag{11}$$

and Ω_{ij} is the mean vorticity tensor, defined by

$$\Omega_{ij} = \frac{1}{2}\left(\frac{\partial \langle u_i \rangle}{\partial x_j} - \frac{\partial \langle u_j \rangle}{\partial x_i} \right) \tag{12}$$

The constants of the pressure tensor R_{ij} in the SSG model are given in table 1. Finally, the dissipation tensor ε_{ij} is modeled as

$$\varepsilon_{ij} = \frac{2}{3}\delta_{ij}\varepsilon \tag{13}$$

Here ε is the dissipation of turbulent kinetic energy. For flows with high Reynolds numbers equation (13) is valid due to local isotropy (Pope, 2000). A separate transport equation for ε is part of the turbulence model. This equa-

C_{s1}	C_{s2}	C_{r1}	C_{r2}	C_{r3}	C_{r4}	C_{r5}
1.7	-1.05	0.9	0.8	0.65	0.625	0.2

Table 1: Constants of rapid pressure tensor R_{ij} in SSG turbulence model.

tion is given by

$$\frac{\partial \varepsilon}{\partial t} + u_k \frac{\partial \varepsilon}{\partial x_k} = \frac{\partial}{\partial x_k}\left[\left(\nu \delta_{kl} + C_\varepsilon \frac{k}{\varepsilon}\langle u'_k u'_l\rangle\right)\frac{\partial \varepsilon}{\partial x_l}\right] + C_{\varepsilon 1}\frac{P\varepsilon}{k} - C_{\varepsilon 2}\frac{\varepsilon^2}{k} \quad (14)$$

Here the constant are C_ε = 0.18, $C_{\varepsilon 1}$ = 1.45 and $C_{\varepsilon 2}$ = 1.83.
In the experimental setup a flow straightener is mounted. To model the effects of the elimination of the swirl on the upstream flow field the flow straightener is numerically modeled as a porous region. The porous region is characterized by its porosity γ and the momentum loss term S_m. In the porous domain the single-phase flow equations are given by

$$\nabla.(\gamma \mathbf{u}) = 0 \quad (15)$$

$$\gamma \frac{\partial(\mathbf{u})}{\partial t} + \gamma \mathbf{u}.\nabla \mathbf{u} = -\gamma \frac{\nabla p}{\rho} + \gamma \nu \nabla^2 \mathbf{u} + \gamma \mathbf{g} \quad (16)$$

$$- \gamma \nabla.\langle \mathbf{u}'\mathbf{u}'\rangle + \frac{\gamma}{\rho}\mathbf{S}_m \quad (17)$$

At the interfaces between the fluid and the porous regions a jump in porosity is present. Across the interface the mass and the momentum fluxes are conserved. The porosity γ is defined as the fraction of the volume occupied by the fluid. For this flow straightener the porosity is $\gamma = 0.2667$. The reduction in flow area leads to a substantial increase in velocity. The momentum loss term S_m represents the inertial loss contribution, which depends on the square of the fluid velocity

$$S_m = -\mathbf{K}_{loss}\frac{\rho}{2}|\mathbf{u}|\mathbf{u} \quad (18)$$

The axial loss coefficient of $\mathbf{K}_{loss}$ is estimated from pressure drop measurements and pipe flow theory. Also the transverse components of the parameter $\mathbf{K}_{loss}$ are set a factor ten higher than the axial component to ensure the suppression of the radial and azimuthal velocity components. The loss parameter $\mathbf{K}_{loss}$ is given by

$$\mathbf{K}_{loss} = \begin{bmatrix} 120 & 0 & 0 \\ 0 & 120 & 0 \\ 0 & 0 & 12 \end{bmatrix} [m^{-1}] \quad (19)$$

Two-phase flow

The high volume fraction of the dispersed oil phase demands the use of the two-fluid model for the calculation of the two-phase flow. This two-fluid model is also called the Euler-Euler model. The model is obtained by volume or time-averaging of the two-phase flow, in which it is assumed that the averaging volume is large enough or the averaging time scale is long enough to obtain a meaningful average of the non-uniformities in the flow. For a thorough derivation the reader is referred to Prosperetti and Tryggvason (2007) or Drew (1983). In the resulting model both phases are represented as interpenetrating fluids, with only the volume fraction indicating the relative fractions of the phases at that location. For both phases separate continuity and momentum equations part of the model. These equations are coupled by an interfacial momentum transfer term M. The continuity equation and the momentum equations for phase k are given by

$$\frac{\partial \alpha_k}{\partial t} + \nabla \cdot (\alpha_k \mathbf{u}_k) = 0 \quad (20)$$

$$\rho_k \alpha_k \frac{D\mathbf{u}_k}{Dt} = -\alpha_k \nabla p + \nabla \cdot (\alpha_k \sigma) + \alpha_k \rho_k \mathbf{g} \quad (21)$$

$$+ \rho_k \nabla \cdot (\alpha_k \langle \mathbf{u}'_k \mathbf{u}'_k\rangle) + \mathbf{M}_k \quad (22)$$

Here α_k is the volume fraction of phase k and the material derivative is defined as

$$\frac{D\mathbf{u}_k}{Dt} = \frac{\partial \mathbf{u}_k}{\partial t} + (\mathbf{u}_k \cdot \nabla)\mathbf{u}_k \quad (23)$$

Both phases share the same pressure field and therefore the phase subscript of the pressure is dropped. The viscous stress tensor is given by

$$\sigma = \mu_k(\nabla \mathbf{u}_k + (\nabla \mathbf{u}_k)^T) \quad (24)$$

M_k is the interfacial momentum transfer, which is the fluid dynamics force acting on phase k. Here surface tension effects are neglected and therefore $M_w = -M_o$, where the subscripts w and o indicate water and oil, respectively.
The momentum transfer term models the physics of the interaction of the phases. Currently, only the drag force is incorporated. In the derivation of the drag force the water phase is defined as continuous and the oil phase as dispersed. The expression for the drag force acting on the water phase is given by

$$M_w = \frac{3}{4}\frac{C_D}{D}\rho_w \alpha_o \mid \mathbf{u}_o - \mathbf{u_w} \mid (\mathbf{u}_o - \mathbf{u}_w) \quad (25)$$

The C_D is the drag coefficient and D is the diameter of the oil droplets. The drag law formulations by Schiller and Naumann (1933) and by Ishii and Zuber (1979) are considered in the present study. The correlation of Schiller and Naumann (1933) is defined by

$$C_D = \frac{24}{Re_D}(1 + 0.15 Re_D^{0.687}) \quad (26)$$

Here Re_D is the Reynolds number based on the relative velocity:

$$Re_D = \frac{\rho_w \mid \mathbf{u_o} - \mathbf{u_w} \mid D}{\mu_w} \quad (27)$$

This correlation is applicable to spherical droplets for Reynolds numbers up to 1000. However, equation (26) does not take into account the hinderance effect other droplets have on the movement of a droplet.
In the expression by Ishii and Zuber this effect is modeled by basing the Reynolds number on the mixture viscosity. The viscosity of the water in equation (27) is therefore

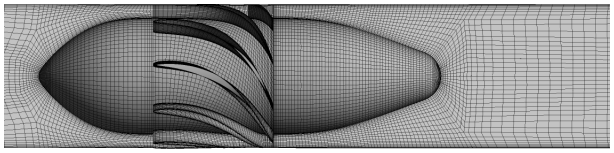

Figure 3: Mesh on the surface of the ISE and on the plane through the axis on the separator. 1.4M hexahedral elements are used for the mesh.

replaced by

$$\mu_m = \mu_w(1-\alpha_o)^{-2.5\frac{\mu_o+0.4\mu_w}{\mu_o+\mu_w}} \quad (28)$$

As a droplet moves through the fluid it will induce a motion of the continuous phase and thereby deform the surrounding fluid. When other droplets are present in this surrounding fluid they will be subjected to this deformation as well. Due the Laplace pressure, the surrounding droplets will resist deformation more than the continuous fluid, leading to a higher perceived viscosity experienced by the moving droplet. Therefore the drag for these dense systems is modeled by assuming similarity to the single droplet case and increasing the viscosity.
In addition to the pressure field, in the two-phase computation both phases share the turbulence field, that is at a certain location the Reynolds stresses and the turbulent dissipation are identical for both phases. Since the phases will separate the use of a different turbulence model for the dispersed phase is not advised. As for the single-phase flow here the SSG model is used to model the turbulence in both phases.

Computational method

The governing equations were solved using the commercial CFD package Ansys CFX 12.1, which uses a cell-centered finite-volume method. The CFX solver uses a co-located grid in which the discrete values of the pressure and velocity components are computed at the same location. The spatial and temporal discretizations are second-order accurate.
A computational mesh has been generated which consists of 1.4 million hexahedral elements. Figure 3 shows the mesh on the surface of the ISE and on the plane through the axis of the separator.
Near the walls the mesh is refined in order to capture the near wall behavior of the flow. To reduce the computational requirements wall functions are employed to represent the flow structure in the region adjacent to the wall. Wall functions use empirical relations to impose the wall shear stress at the nodes next to the wall, which are all located outside the viscous sublayer.
At the inlet the bulk axial velocity u_b is 2 m/s, leading to a flow rate of 56.5 m^3/hr. At the oil outlet a mass flow boundary condition of 30wt% of the inlet flow is imposed. At the water outlet an averaged reference pressure of 0 Pa is imposed. The density of the water and the oil is 1067.8 kg/m^3 and 869 kg/m^3, respectively. A mono-dispersed oil phase is assumed with a droplet diameter D = 100 μm. The dynamic viscosity of the the water and the oil is 1.183x10^{-3} kg/ms and 8.690x10^{-3} kg/ms, respectively.
The transient simulations are run until an operational state is established. In this operational state the mean velocity **u** varies in a periodic fashion around some final mean value. After this state has established, the time-averaged values of the mean velocity and other quantities are calculated using sufficient time steps to capture several periods of the periodic solution.

SINGLE-PHASE FLOW RESULTS

Downstream of the ISE a strongly swirling flow is present. The generation of the swirling flow is accompanied by a pressure drop in the axial direction of 1.5x10^5 Pa. For the calculation of this pressure difference, the pressure is averaged over the cross-sectional planes just up- and just downstream of the ISE.
The time-averaged axial and azimuthal velocity on a plane through the axis of the separator are seen in figure 4. In the plot of the axial velocity, an annular region of re-

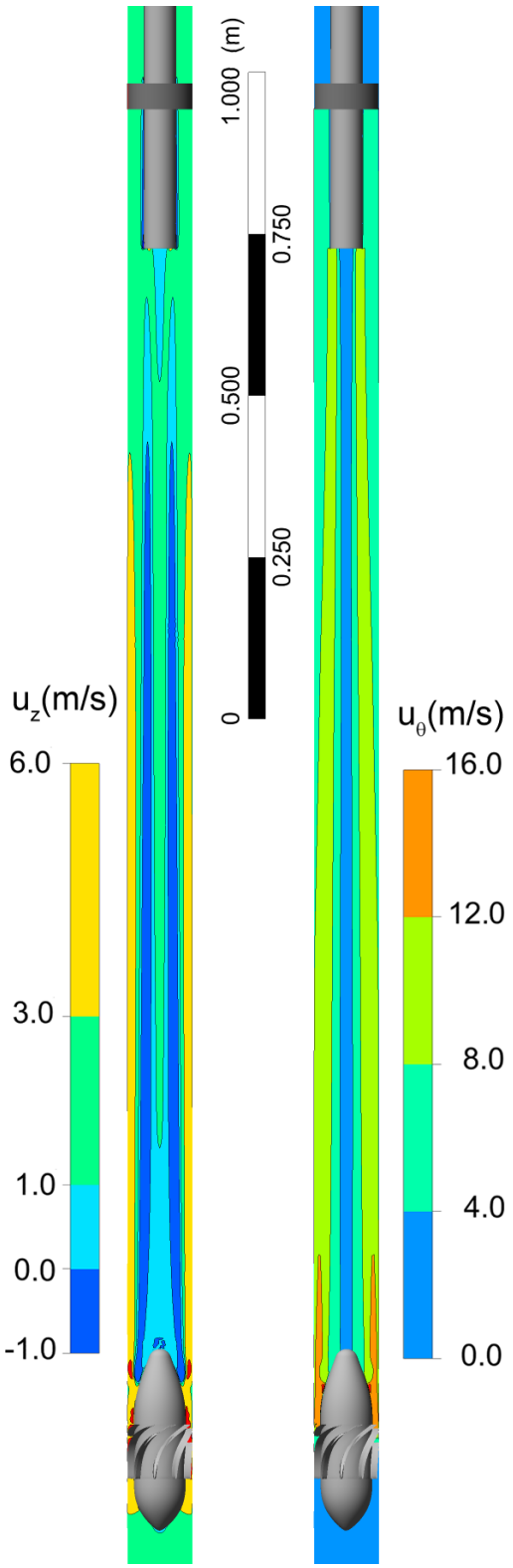

Figure 4: Contours of time-averaged velocities on plane through the axis of the separator for flow of single-phase water: axial velocity (left) and azimuthal velocity (right).

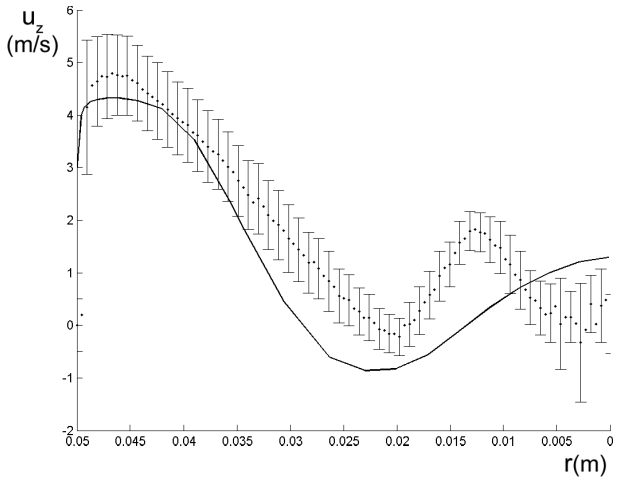

(a) Axial velocity

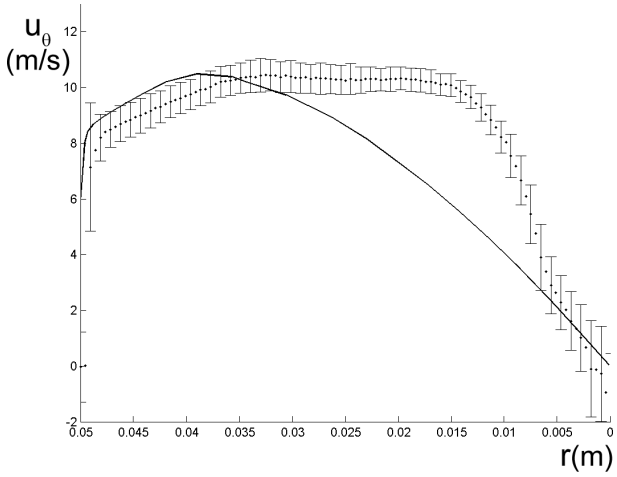

(b) Azimuthal velocity

Figure 5: Comparison of radial distribution of time-averaged axial and azimuthal velocity at 0.44 m downstream of the ISE of numerical (solid) and experimental (dotted) results, error bars give standard deviation of measurements around mean value. Results for half the pipe diameter are shown.

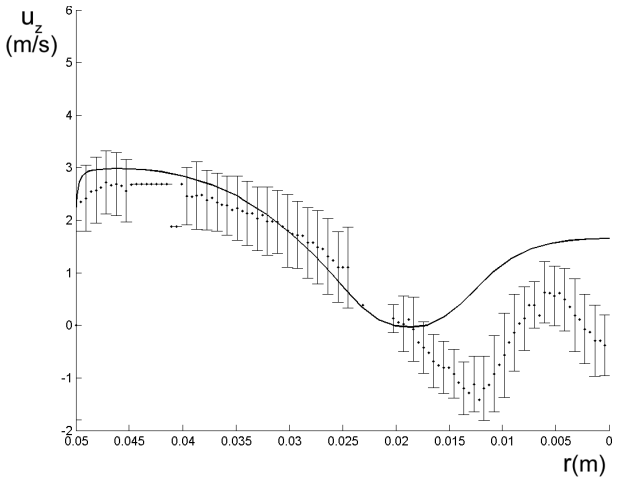

(a) Axial velocity

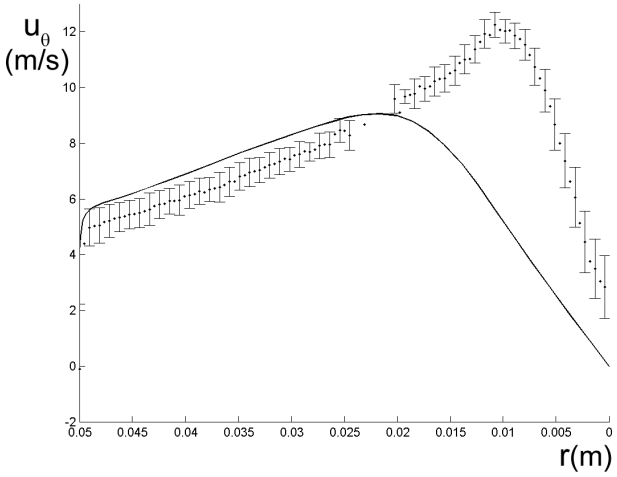

(b) Azimuthal velocity

Figure 6: Comparison of radial distribution of time-averaged axial and azimuthal velocity at 1.395 m downstream of the ISE of numerical (solid) and experimental (dotted) results, error bars give standard deviation of measurements around mean value. Results for half the pipe diameter are shown.

versed flow can be seen surrounded by a regions with positive axial velocity near the pipe wall and one around the center of the pipe, resulting in a W-shaped radial distribution of the axial velocity. This reversed flow pattern has been observed before (Mattner *et al.*, 2002; Ko, 2005). In downstream direction, the axial velocity decreases in the region near the pipe wall and becomes less negative in the annular reversed flow region. In the region at the center of the pipe the axial velocity increases further downstream. Just upstream of the pick-up tube a distinct change in flow pattern is obversed. In the center a decrease in the axial velocity is seen, while the axial velocity increases in the region near the inner wall of the pick-up tube. Still further downstream, inside the pick-up tube, the W-shaped radial distribution of the axial velocity is recovered. Furthermore, a second reversed flow region is observed in the region next to the outer surface of the pick-up tube. All three effects are features of the swirling flow and are not seen in case of non-swirling flow. The porous region emulating the flow straightener is indicated by the dark grey ring in the figure 4. Due to the obstruction of the flow the axial velocity experiences a sharp increase inside the flow straightener.

The highest azimuthal velocity can be seen just downstream of the ISE, reaching velocities up to 16 m/s. Initially, the azimuthal velocity decreases rapidly, but further downstream the rate of decay of the swirl decreases. The azimuthal velocity remains higher than 8 m/s for most of the separator volume. In downstream direction the location of the maximum in the radial distribution of the azimuthal velocity moves towards the center of the pipe. Near the pick-up tube the flow converges, leading to centrifugal accelerations of 600 g near the pick-up tube opening.

Although obscured by the time-averaging, a mild vortex core precession of the flow is seen, that is a low-amplitude time-dependent motion of the vortex core around the geometrical axis of the pipe. The vortex core precessing is strongest just aft of the ISE, further downstream it decreases. The reduction in vortex core precessing may be attributed to the pick-up tube which appears to have a stabilizing effect on the flow.

The numerical and experimental results for the radial distribution of the time-averaged axial and azimuthal velocity along a line through the center in the cross-sectional plane at z = 0.44 m and 1.395 m downstream of the ISE are compared in the figures 5 and 6, respectively.
Currently, in the experimental setup a gas core with a diameter of about 10 mm is present. This more or less stagnant gas core is likely to considerably influence the velocity profile of the liquid phases near the center. Moreover, for the LDA system it is difficult to measure through the gas core. Since the optical transition between the PMMA pipe wall and the water causes refraction, measurements are only done along lines passing through the center of the pipe. Therefore, only the velocity distributions for half the pipe diameter, from the pipe wall to the center are presented here.
The numerical results predict the axial flow pattern well, except for the 10 mm near the center as can be observed in figure 5(a). Both the predicted high axial velocity near the wall and the reversed flow region are confirmed by the experiments. In the center the experiments show a second local minimum, while the numerical results show a local maximum in axial velocity. Moreover, the experiments show an overall higher axial velocity and therefore a higher mass flow compared to the mass flow prescribed in the numerical simulations. This may be explained by asymmetries in the flow field in the experimental setup. The axial velocity on the other side of the gas core should therefore be lower than the axial velocity found in the computation.
The azimuthal velocity in figure 5(b) shows good agreement in the near wall region. Further inward, the experiments show a much higher azimuthal velocity, indicating a relatively narrow region with strong axial vorticity. In the results of the numerical simulation the vorticity is at a lower level and is distributed over a larger region.
Further downstream, at z = 1.395 m, the agreement is very satisfactory for radial locations above 20 mm. Closer to the center the differences become large. While the numerical solution indicates the end of the annular reversed flow region, the experiments show a further decrease in axial velocity of the reversed flow compared to the situation at the upstream station at z = 0.44 m. Furthermore, the experiments show a higher peak in the azimuthal velocity. The maximum is located closer to the center compared to the upstream situation, leading to a much larger velocity gradient.
Apart from the region near the center of the pipe, there is good qualitative agreement between the measurements and the results from numerical flow simulations. However, the influence of the gas core on the velocity field is unknown and is very likely to contribute to the differences in the results. Efforts will be made in the future to remove the gas core.

TWO-PHASE FLOW RESULTS

Simulations of two-phase flow have been carried out to study the oil-water flow in the separator and to assess the predicted separation efficiency for different drag law formulations. The inlet oil volume fraction is set to 0.25, representing a feed from a high watercut oil field. The mass flow split through the oil outlet is again set to 0.3. The mass fraction of oil at the inlet is lower than 0.3, therefore this mass flow setting will likely result in cleaner water at the water outlet rather than purer oil at the oil outlet. The drag law correlation of Schiller and Naumann (1933) and that of Ishii and Zuber (1979) are used in the modeling of the interfacial drag between the oil and water phase.
The solution indeed shows the successful bulk separation

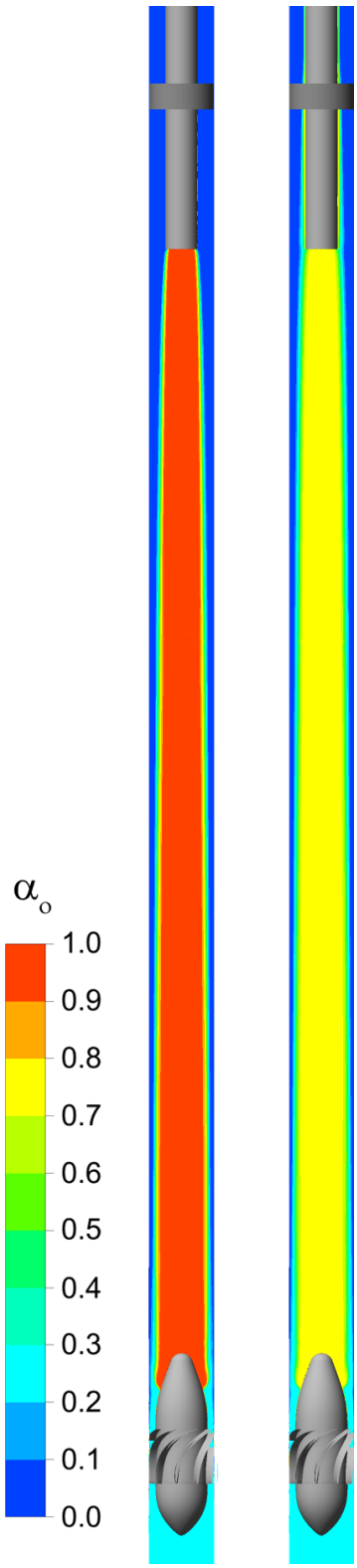

Figure 7: Contours of time-averaged oil volume fraction on plane through the axis of the separator for Schiller-Naumann (left) and Ishii-Zuber (right) drag laws. Inlet volume fraction is 25%.

of the phases. The oil volume fraction in the separator is shown in figure 7, the left subfigure shows the results for the Schiller-Naumann drag law and the right subfigure shows the results for the drag law by Ishii and Zuber. A large difference in the distribution of the volume fraction is observed. For the Schiller-Naumann case, a large central region of pure oil can be seen. Oil will accumulate in the separator, leading to a hold-up of 42%. Almost all the oil is captured by the pick-up tube. The distribution of the oil volume fraction is different for the case for which the Ishii-Zuber drag law has been applied. Also in this case oil accumulates in the center of the separator leading to a hold-up of 38%. However, the oil volume fraction only reaches a value of about 80%. The oil volume fraction does not appear to increase to values higher than this 80%. Also some oil can be seen to spill over the pick-up tube, flowing towards the water outlet.
The reason for this behavior can be found in the definition of the mixture viscosity μ_m in equation (28). The ratio of mixture viscosity to water viscosity is given as function of the oil volume fraction α_o in figure 8. The mixture viscosity is increasing rapidly as the oil volume fraction increases above 0.6. For instance, at an oil volume fraction of 0.80 the mixture viscosity is already 40 times as high as the water viscosity. Since M_k increases with the mixture viscosity, the resulting velocity difference between the oil and the water will become very small. Therefore, further separation is prevented and the oil volume fraction is limited. Ishii and Zuber claim their drag relation can be used for dispersed volume fractions up to 0.95 if the dispersed phase is a gas or liquid. However, in a real application it is likely that at lower oil volume fractions coalescence between the droplets will occur. At a certain point phase inversion will occur and water will become the dispersed phase. However, in the current drag formulation the oil is treated as the dispersed phase, regardless of the value of the volume fraction.
It appears that the Schiller-Naumann drag law will overestimate the radial velocity of the dispersed phase since it cannot account for the mutual interferences of droplets moving towards the center of the pipe. Moveover, the Ishii-Zuber drag law will impose a maximum oil volume fraction due to its inability to incorporate phase inversion.

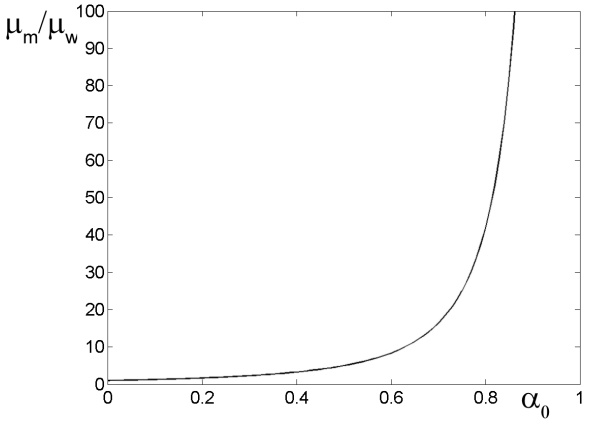

Figure 8: The ratio of mixture viscosity μ_m to water viscosity μ_w given as function of the oil volume fraction α_o

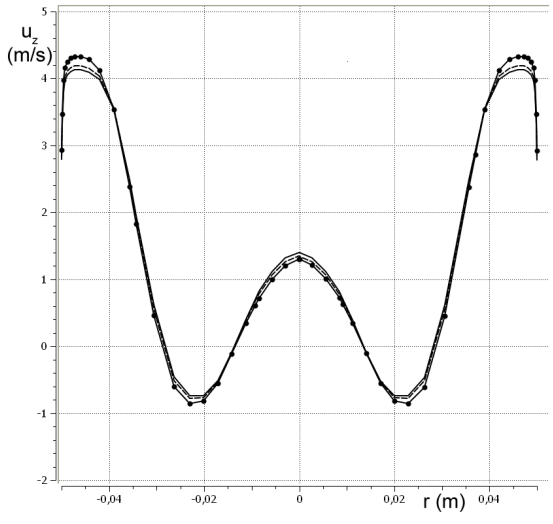

(a) z = 0.44 m

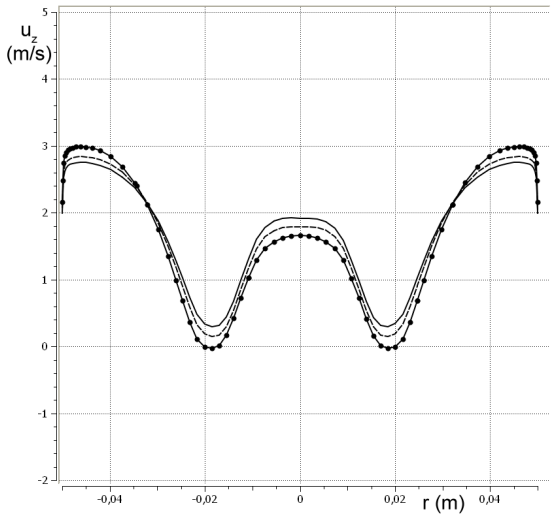

(b) z = 1.395 m

Figure 9: Comparison of radial distribution of time-averaged axial water velocity at z = 0.44 m and z = 1.395 m for single-phase flow (solid with dots), two-phase flow with Schiller-Naumann drag law (dashed) and two-phase flow with Ishii-Zuber drag law (solid).

The separation efficiency is defined as the ratio of the oil mass flow rate through the oil outlet to the oil mass flow rate at the inlet. When the Schiller-Naumann drag relation is applied the separation efficiency is 98%. The separation efficiency for the case in which the Ishii-Zuber relation is used is lower, as expected: 89%. Another important result from the simulation is the oil volume fraction at the water outlet, this is 0.7% and 4% when using the Schiller-Naumann and Ishii-Zuber drag law, respectively. Current experimental results indicate the separation efficiency to be about 65%. Therefore, it appears that in both cases the numerical simulations substantially overestimate the separation efficiency. This may partially be attributed to discrepancies in the input parameters of the numerical simulations and those of the experiments. For instance, the mass flow split in the experiments is lower than the one in the numerical simulations and the droplet sizes at inlet differ. However, the main reason for the difference in separation efficiency is

expected to be the effect of turbulence on the segregation of the dispersed phase which is not taken into account. Therefore, a suitable turbulent dispersion model should be incorporated in the interfacial momentum transfer term in future work.

The radial distribution of time-averaged axial water velocity for single-phase flow, two-phase flow with the Schiller-Naumann drag law and with the Ishii-Zuber drag law at z = 0.44 m and z = 1.395 m are shown in figure 9. The difference between the axial velocity of the phases is negligible compared to the magnitude of the axial velocity. Therefore only the water velocity is shown here. At z = 0.44 m the differences in axial water velocity obtained for the three flow simulations is small. The differences in the azimuthal water velocity are even smaller and are therefore not shown here. It appears that the introduction of a second phase has little effect on the axial velocity field. The similar velocity distribution for both two-phase flow simulations indicate that only the radial movement of the oil phase is affected by the higher drag coefficient of the Ishii-Zuber drag relation. In the axial and azimuthal direction the differences in the velocity of the oil and the water is only a fraction of the total velocity. So any changes in these slip velocities will be hardly visible. Furthermore, due to the high Reynolds number of these flows, the effect of the higher viscosity of the oil on the velocity field is likely to be small. Although the velocity fields are very similar, the single-phase flow simulation showed a 10% higher pressure drop over the ISE cause by the higher density of the water compared to the mixture.

Further downstream, at z = 1.395 m, the differences in velocity are larger. This difference can be explained by changes in the volume flow split. Although the mass flow split is set to 0.3 in all simulations, the volume flow split differs due to changes in composition of the mixture at the outlet. The largest quantity of oil is extracted through the oil outlet in the two-phase flow case with the Schiller-Naumann drag law. Consequently, the highest axial water velocities can be seen for that case. The opposite is true for the single-phase flow simulation, leading to the lowest axial water velocities in the center region of the pipe. Since the volume rates at the inlet are equal for all three cases the axial velocities in the near wall region show to opposite behavior.

CONCLUSIONS

An in-line oil-water separator has been designed and is investigated for both single- and two-phase flow. The separator consists of an internal swirl element (ISE), which uses vanes to generate the swirling flow by deflecting the flow. Downstream a pick-up tube is placed to collect the separated oil stream. In the separator a strongly swirling flow is seen with an annular reversed flow region.

The predicted single-phase flow field has been compared to LDA measurements of the flow in the experimental setup of the separator at Delft University of Technology. The agreement between numerical and experimental results is satisfactory in the region near the wall. However, near the center of the pipe large differences are seen. In the experimental setup an gas core was observed, which negatively influences the comparison.

Two-phase flow simulations have been carried out to study the flow field of an oil-water mixture in the separator. In addition, different drag laws were employed to investigate their effect on the flow field and on the separation efficiency. In the region downstream of the ISE the oil accumulates, leading to an oil hold-up of about 40%. The use of the drag law by Schiller and Naumann results in a core of pure oil, which is subsequently extracted with little spill-over. In the two-phase flow simulation which used the drag law by Ishii and Zuber the oil volume fraction in the separator did not increase beyond about 80%. Considerable spill-over was seen for this case. The two-phase flow simulations overestimate the separation efficiency by more than 20% when compared to the experimental results. Finally, the velocity field in the two-phase flow simulation was found to be very similar to that resulting from the single-phase flow computation.

ACKNOWLEDGEMENTS

This is an Institute for Sustainable Process Technology (ISPT) project. This research is part of project Oil & Gas 00-004.

REFERENCES

BELT, R. (2007). *On the liquid film in inclined annular flow*. Ph.D. thesis, Delft University of Technology.

BRADLEY, D. (1965). *The Hydrocyclone*. Pergamon Press.

CHEN, J. and LIN, C. (1999). "Computations of strongly swirling flows with second-moment closures". *International Journal for Numerical Methods in Fluids*, **30**, 493–508.

CULLIVAN, J. *et al.* (2003). "Understanding the hydrocyclone separator through computational fluid dynamics". *Transactions Institution of Chemical Engineers A*, **81**, 455–466.

DALY, B. and HARLOW, F. (1971). "Transport Equations in Turbulence". *Physics of Fluids*, **13**, 2634–2649.

DELFOS, R. *et al.* (2004). "A design tool for optimising axial liquid-liquid hydrocyclones". *Minerals Engineering*, **17(5)**, 721–731.

DERKEN, J. (2003). "Separation performance predictions of a stairmand high-efficiency cyclone". *American Institute of Chemical Engineers Journal*, **49(6)**, 1359–1371.

DIRKZWAGER, M. (1996). *A New Axial Cyclone Design for Fluid-Fluid Separation*. Ph.D. thesis, Delft University of Technology.

DREW, D. (1983). "Mathematical modeling of two-phase flow". *Annual Review of Fluid Mechanics*, **15**, 261–291.

HANJALIC, K. (1999). "Second-Moment Turbulence Closures for CFD: Needs and Prospects". *International Journal of Computational Fluid Dynamics*, **12(1)**, 67–97.

HOEKSTRA, A.J. (2000). *Gas Flow Field and Collection Efficiency of Cyclone Separtors*. Ph.D. thesis, Delft University of Technology.

ISHII, M. and ZUBER, M. (1979). "Drag coefficient and relative velocity in bubbly, droplet or particulate flows". *AIChE J*, **25**.

KHAROUA, N. *et al.* (2010). "Hydrocyclones for de-oiling applications-a review". *Petroleum Science and Technology*, **28**, 738–755.

KITOH, O. (1991). "Experimental study of turbulent

swirling flow in a straight pipe". *Journal of Fluid Mechanics*, **225**, 445–479.

KO, J. (2005). *Numerical modelling of highly swirling flows in a cylindrical through-flow hydrocyclone*. Ph.D. thesis, Royal Institute of Technology.

MANNINEN, M. and TAIVASSALO, V. (1996). "On the mixture model for multiphase flow". Tech. rep., Technical Research Centre of Finland.

MATTNER, T. *et al.* (2002). "Vortical flow. part 1. flow through a constant-diameter pipe". *Journal of Fluid Mechanics*, **463**, 259–291.

MURPHY, S. *et al.* (2007). "Prediction of strongly swirling flow within an axial hydrocyclone using two commercial CFD codes". *Chemical engineering science*, **62**, 1619–1635.

NOROOZI, S. and HASHEMABADI, S. (2009). "CFD simulation of inlet design effect on deoiling hydrocyclone separation efficiency". *Chemical Engineering and Technology*, **32(12)**, 1885–1893.

PALADINO, E. *et al.* (2007). "Developing multiphase models for liquid-liquid hydrocyclone flow". *6th International Conference on Multiphase Flow*, S6 Wed C 37.

POPE, S.B. (2000). *Turbulent Flows*. Cambridge University Press.

PROSPERETTI, A. and TRYGGVASON, G. (2007). *Computational Methods for Multiphase Flow*, chap. Averaged equations for multiphase flow, 237–282. Cambridge University Press.

SCHILLER, L. and NAUMANN, A. (1933). "Uber die grundlegenden berechnungen bei der schwerkraft aufbereitung". *Zeitschrift des Vereines Deutscher Ingenieure*, **77**, 318.

SPEZIALE, C. *et al.* (1991). "Modelling the pressure-strain correlation of turbulence: an invariant dynamical systems approach". *Journal of Fluid Mechanics*, **227**, 245–272.